

Article

Satellite Observations for Detecting and Forecasting Sea-Ice Conditions: A Summary of Advances Made in the SPICES Project by the EU's Horizon 2020 Programme

Marko Mäkinen ^{1,*}, Jari Haapala ¹, Giuseppe Aulicino ², Beena Balan-Sarojini ³, Magdalena Balmaseda ³, Alexandru Grgic ¹, Fanny Girard-Ardhuin ⁴, Stefan Hendricks ⁵, Georg Heygster ⁶, Larysa Istomina ⁵, Lars Kaleschke ⁵, Juha Karvonen ¹, Thomas Krumpen ⁵, Mikko Lensu ¹, Michael Mayer ^{3,7}, Flavio Parmiggiani ⁸, Robert Ricker ^{4,5}, Eero Rinne ¹, Amelie Schmitt ⁹, Markku Similä ¹, Steffen Tietsche ³, Rasmus Tonboe ¹⁰, Peter Wadhams ¹¹, Mai Winstrup ¹² and Hao Zuo ³

¹ Finnish Meteorological Institute, PB 503, FI-00101 Helsinki, Finland; jari.haapala@fmi.fi (J.H.); alexandru.grgic@fmi.fi (A.G.); juha.karvonen@fmi.fi (J.K.); mikko.lensu@fmi.fi (M.L.); eero.rinne@fmi.fi (E.R.); markku.simila@fmi.fi (M.S.)

² Department of Science and Technology—DiST, Università degli Studi di Napoli Parthenope, Centro Direzionale Is C4, 80143 Napoli, Italy; giuseppe.aulicino@unipARTHENOPe.it

³ European Centre for Medium-Range Weather forecasts, Shinfield Park, Reading RG2 9AX, UK; beena.sarjojini@ecmwf.int (B.B.-S.); magdalena.balmaseda@ecmwf.int (M.B.); michael.mayer@ecmwf.int (M.M.); steffen.tietsche@ecmwf.int (S.T.); hao.zuo@ecmwf.int (H.Z.)

⁴ Ifremer, Univ. Brest, CNRS, IRD, Laboratoire d'Océanographie Physique et Spatiale, IUEM, 29280 Brest, France; fanny.ardhuin@ifremer.fr

⁵ Alfred Wegener Institute, Am Handelshafen 12, 27570 Bremerhaven, Germany; stefan.hendricks@awi.de (S.H.); larysa.istomina@awi.de (L.I.); lars.kaleschke@awi.de (L.K.); thomas.krumpen@awi.de (T.K.); robert.ricker@awi.de (R.R.)

⁶ Institute of Environmental Physics, University of Bremen, 28359 Bremen, Germany, (now consultant at the same institute); heygster@uni-bremen.de

⁷ Department of Meteorology and Geophysics, University of Vienna, UZA II, Althanstrasse 14, 1090 Vienna, Austria

⁸ Department of Satellite Meteorology, ISAC-CNR, Via Piero Gobetti 101, 40129 Bologna, Italy; f.parmiggiani@isac.cnr.it

⁹ Faculty of Mathematics, Informatics and Natural Sciences, University of Hamburg, Bundesstr. 53, 20146 Hamburg, Germany; amelie.schmitt@uni-hamburg.de

¹⁰ Danish Meteorological Institute, Lyngbyvej 100, 2100 Copenhagen, Denmark; rtt@dmi.dk

¹¹ Department of Life and Environmental Sciences—DiSVA, Università Politecnica delle Marche, Via Brecce Bianche, 60131 Ancona, Italy; pw11@cam.ac.uk

¹² DTU Space, National Space Institute, Technical University of Denmark, Elektrovej Bygning 327, 2800 Kongens Lyngby, Denmark; maiwin@space.dtu.dk

* Correspondence: marko.makynen@fmi.fi; Tel.: +358-50-5687758

Received: 25 February 2020; Accepted: 7 April 2020; Published: 10 April 2020



Abstract: The detection, monitoring, and forecasting of sea-ice conditions, including their extremes, is very important for ship navigation and offshore activities, and for monitoring of sea-ice processes and trends. We summarize here recent advances in the monitoring of sea-ice conditions and their extremes from satellite data as well as the development of sea-ice seasonal forecasting capabilities. Our results are the outcome of the three-year (2015–2018) SPICES (Space-borne Observations for Detecting and Forecasting Sea-Ice Cover Extremes) project funded by the EU's Horizon 2020 programme. New SPICES sea-ice products include pancake ice thickness and degree of ice ridging based on synthetic aperture radar imagery, Arctic sea-ice volume and export derived from multisensor satellite

data, and melt pond fraction and sea-ice concentration using Soil Moisture and Ocean Salinity (SMOS) radiometer data. Forecasts of July sea-ice conditions from initial conditions in May showed substantial improvement in some Arctic regions after adding sea-ice thickness (SIT) data to the model initialization. The SIT initialization also improved seasonal forecasts for years with extremely low summer sea-ice extent. New SPICES sea-ice products have a demonstrable level of maturity, and with a reasonable amount of further work they can be integrated into various operational sea-ice services.

Keywords: Arctic; sea ice; remote sensing; forecasting

1. Introduction

The detection, monitoring, and forecasting, both in short and seasonal time scales, of sea-ice conditions and their extremes is very important for ship navigation and offshore activities, and also for monitoring of sea-ice processes and trends. In the simplest case, operations of non-ice class vessels require real-time observation and forecasts of sea-ice edge position only, but tactical navigation of ice-strengthened ships needs detailed information such as sea-ice thickness (SIT) variability on a local scale. Ships and structures are usually designed to resist typical forces induced by pack ice, but they are not designed to resist extreme sea-ice conditions. Hence, also observations of the thickest and strongest ice types, pressure ridges, thick windrow/brash ice layers, existence of multiyear ice (MYI), and icebergs, which are considered local SIT extremes, become elementary monitoring parameters for risk management in ice-covered waters. The aforementioned hazards for shipping are meters to kilometre-scale features and can be avoided by an ice navigator. Anomalous ice conditions in a certain region at a certain time can also give rise to extreme conditions that may impact navigation and planning hereof. These events are larger in scale, 100–1000 kilometres in spatial scale and may last months to seasons in their temporal impact.

Currently available sea-ice products for shipping and offshore activities and for monitoring of sea-ice processes and trends can be categorized as follows: (1) Traditional ice charts showing ice information with the World Meteorological Organization (WMO) sea-ice nomenclature [1]. The charts are produced by national ice services and have typically regional coverage, e.g., surrounding Greenland. (2) Global products showing sea-ice concentration (SIC), ice edge, SIT, ice types (e.g., first-year ice (FYI) versus MYI), snow thickness on sea ice, melt pond fraction (MPF), or ice drift. The resolution of the products is typically 5 to 30 km. They are mostly based on microwave radiometer, radar altimeter and scatterometer data. In some products, like ice drift, also synthetic aperture radar (SAR) data are used. (3) Regional or limited coverage products based mainly on the SAR imagery. During summertime also fine resolution (~10–100 m) optical imagery can be utilized. These include ice type charts, ice drift, degree of ice ridging, iceberg charts, MPF, and landfast ice extent. (4) Sea-ice forecast products for SIT, SIC, ice drift, etc., with some of the sea-ice models assimilating satellite data [2–4]. The large-scale products in the categories (1), (3) and (4) can be used for strategic planning of shipping and offshore activities, whereas for tactical planning (e.g., ship routing) in the local scale (~100–1000 m) category (3) and (4) products are needed.

For tactical planning several days ahead and for strategic planning months ahead, e.g., to decide when it is possible to sail the Northern Sea Route with a specific ice class vessel, reliable sea-ice forecasts are naturally required. Present numerical weather and climate prediction models include representation of large-scale physical processes of sea ice [5,6]. This makes it possible in principle to predict how sea-ice conditions will evolve in response to predicted weather patterns and seasonal anomalies. These forecasts of ice conditions—from days to several months ahead of time—can provide guidance for strategic and tactical planning of marine activities in the Arctic. Presently, these models are often initialized using satellite observations of SIC, but other sea-ice parameters may be possible to include for producing better forecasts. Recent advances in satellite observations of sea ice, like

SIT, as well as MPF and snow properties on sea ice, have opened up exciting possibilities to improve physical forecast models and their initial conditions [7,8].

In this paper, we summarize recent advances in detection of sea-ice conditions and their extremes, both on global and regional scales, from satellite data, as well as development of relevant sea-ice seasonal forecasting capabilities. They are the outcomes of the three-year (2015–2018) SPICES (Space-borne Observations for Detecting and Forecasting Sea-Ice Cover Extremes) project, funded by the EU’s Horizon 2020 programme [9]. The main objectives of the SPICES were to (1) develop new methods to retrieve sea-ice parameters from existing (and forthcoming) satellite sensors to provide enhanced products for polar operators and prediction systems, specifically addressing extreme and unexpected conditions, and (2) improve capabilities to forecast seasonal sea-ice extremes. Previously, the SPICES results have been presented in detail in 13 peer-reviewed articles and in project reports (available at the European Commission (EC) Community Research and Development Information Service (CORDIS) web-site [9]) focused on a specific SPICES scientific goal. Here, one of goals is to present how the SPICES main results and new products can be interpreted in the context of previous studies and existing products. Future research directions in the monitoring and forecasting of sea-ice conditions are also highlighted. Abbreviations and symbols used in the paper are collected at the end of the paper.

2. New Products of Sea-Ice Conditions

New sea-ice products developed in SPICES are based on a wide variety of Earth Observation (EO) data obtained from multiple satellite sensors, and numerical weather prediction (NWP) model data. For sea-ice product development and validation, a wide variety of in situ snow and sea-ice data was used, as well as some airborne remote-sensing data [10].

Firstly, two products, based on the SAR imagery, are presented, which measure the degree of sea-ice ridging and estimate pancake ice thickness. Next, CryoSat-2 radar altimeter SAR Interferometer Radar Altimeter (SIRAL) data are used to estimate the risk index outcome (RIO) of the International Maritime Organization (IMO) Polar Code. This is followed by a SIT estimation using a combination of the European Space Agency’s (ESA) Soil Moisture and Ocean Salinity (SMOS) and the National Aeronautics and Space Administration (NASA) Soil Moisture Active Passive (SMAP) microwave radiometer (MR) brightness temperature (T_B) data, and furthermore, by a study where multi-sensor satellite data is used to derive sea-ice volume and export. Next, MPF, melt stage, and SIC are estimated using SMOS data which provides daily Arctic coverage unlike optical spectrometer data for the melt parameters. Information on snow depth on sea ice is needed when retrieving SIT from the SIRAL and laser altimeter data, for example. In SPICES, a new snow depth algorithm based on Bayesian inversion of an empirical surface emission forward model was developed. Finally, we look into sea-ice forecasting experiments where the use of the SPICES SIT observations constraining initial conditions led to improved seasonal forecasts during years with extremely low summer sea-ice extents.

2.1. Degree of Sea-Ice Ridging Using Synthetic Aperture Radar (SAR)

One parameter that is important for ship navigation, but which is often not available is the degree of ice ridging (DIR). The estimation of DIR was investigated using RADARSAT-2 C-band SAR dual-polarized HH/HV imagery from the Baltic Sea in Jan–Mar 2013 [11]. Reference DIR values were extracted from the Baltic Sea ice charts prepared by the Finnish Ice Service (FIS). In the charts DIR quantifies ridging-induced navigational difficulty as a numeral estimated by an ice analyst and has the following values: 1 (level ice, slightly rafted ice), 2 (heavily rafted ice, slightly ridged ice), 3 (ridged ice), 4 (heavily ridged ice), 5 (rubble fields, extremely ridged ice, brash ice barriers). Using Baltic Sea ice surface profile data collected in March 2011 with a helicopter-borne lidar instrument, we obtained the following correspondence between the DIR classes and the measured ridge density (0.4 m minimum ridge height): for DIR = 3 on an average 12.7 ridges per 1 nautical mile (NM), and for DIR=4 on average 21.5 ridges per 1 NM. The corresponding average SITs for these DIR categories were 0.76 m and 1.08 m. The simultaneous SIT measurements were made by a helicopter-borne electromagnetic

sensor (HEM). In total lines about 600 km long were measured over an ice area which is covered by the 2013 DIR charts.

The SAR classification procedure for DIR includes two stages. First, the SAR imagery is segmented using the Markov random field paradigm. The sizes of the resulting segments exhibited high variation: the segment sizes varied from 20 km^2 to over $11,000 \text{ km}^2$, the mean of them was about 1000 km^2 . The goal is for the resulting segments to be mainly composed of one DIR category. For each segment a feature vector is computed, that is, a set of SAR image texture features (here 14 features) related to the ice ridging. The second stage classifies every segment using the feature vector and assigns one DIR value to each segment; see an example DIR chart in Figure 1. The classification used a random forest classifier that also assesses the efficiency of each feature in the discrimination. The eight most informative segment-wise features in the classification were used. The training set consisted of charts randomly selected from the three-month period, the rest were used to compare charted DIR values pixel by pixel with the generated DIR classification. The proportions of the ice areas where DIR charts agreed with ice charts varied month by month, being 83%, 63%, and 81% in January, February, and March 2013, respectively.

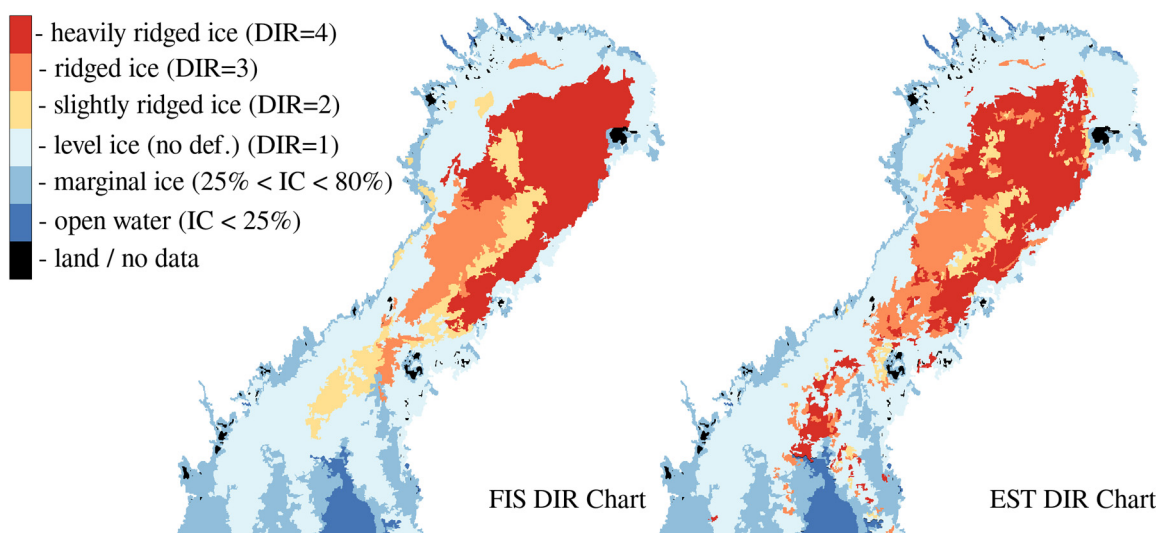


Figure 1. Degree of ice ridging extracted from the digitized Baltic Sea ice charts on 15 March 2013 (left figure). Result of estimated degree of ice ridging based on RADARSAT-2 synthetic aperture radar (SAR) image segmentation and SAR texture classification using a random forest classifier (right figure). Figure from [11].

The method was developed and applied in the Baltic Sea due to the good reference DIR data available. In principle it could also be applied to the seasonal sea-ice regime in the Arctic Ocean. Our plan is to test SAR-based DIR estimation in the Kara Sea using the Baltic Sea ice DIR reference data in the training. The SAR-based DIR charts can be used by ships to aid navigation in the Baltic Sea.

2.2. Determination of Pancake Ice Thickness Using SAR

In fall, the pack ice in both the Antarctic and in critical regions of the Arctic advances by the formation of a mass of floating crystals (frazil ice), which freeze together into pancakes with diameters controlled by the wave field. At larger distances from the ice edge, where the waves are almost completely attenuated by the pancake ice, the pancakes start to freeze together, eventually forming a solid ice sheet. This frazil-pancake cycle is the main way in which the Antarctic ice cover expands. This is also the case for the advancing Beaufort Sea ice edge, as observed in October–November 2015, and for isolated regions of wind-driven coastal polynyas, where an offshore wind creates open water on which frazil-pancake ice forms [12].

The developed SAR-based method derives the thickness of a pancake icefield from the way in which the pancake ice changes the dispersion relation of the waves, dampens the wave amplitude and causes dissipation of the energy of the waves, i.e., it changes the wavelength of ocean waves as they enter the ice [13]. Figure 2a shows an icefield observed from RV Sikuliaq, with a long swell present and a small yellow wave buoy to provide scale. Figure 2b,c show a co-located COSMO-SkyMed X-band SAR image of this ice field. Pancake ice is dark, and open water is the light-coloured area in the centre. Having identified the main direction of the wave energy, a strip of SAR data is divided into five imagettes, or short stretches of image (Figure 2d). For each imagette, a spatial Fourier analysis yields a SAR wave number spectrum, which is inverted to give an energy spectrum [14]. Imagettes 1–3 present a strongly peaked spectrum giving the preferred wavelength and direction (Figure 2e). Imagettes 4–5, extending into open water, have a much wider spectrum. From the change in shape of the spectrum as the waves enter the ice, and by applying a viscous theory for wave propagation in pancake ice, it was estimated that there was an ice thickness of 21 cm in this case, which agreed well with in situ direct observations.

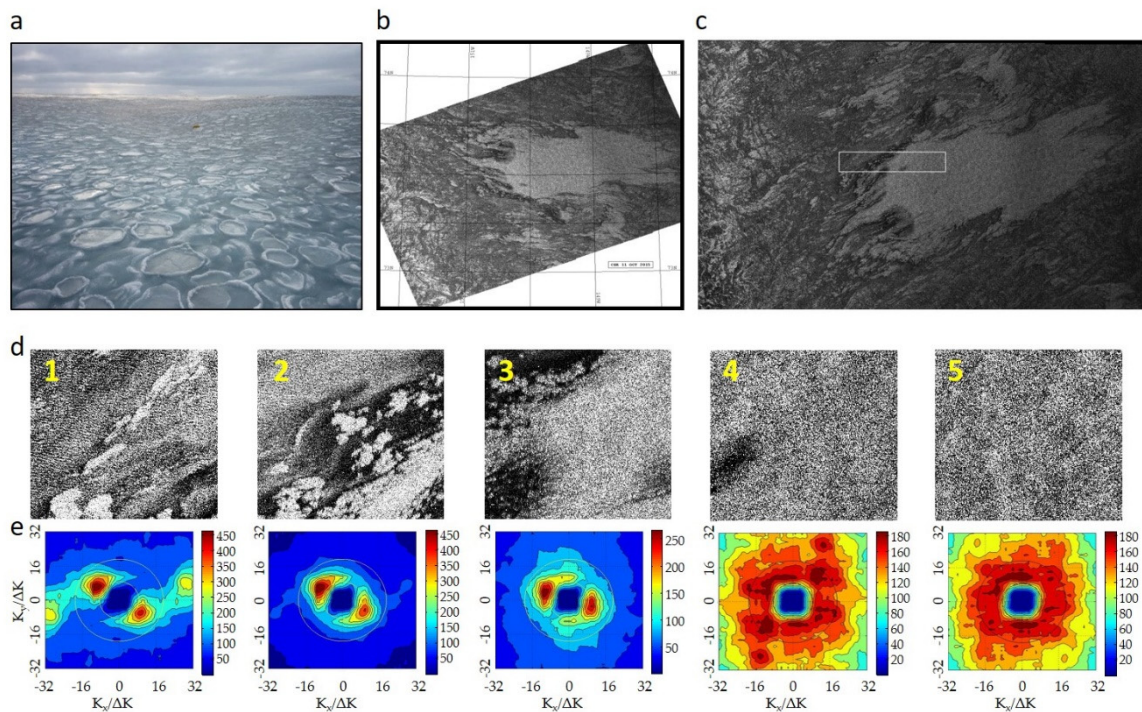


Figure 2. Area of RV Sikuliaq field operations seen from (a) camera and (b) COSMO-SkyMed X-band SAR on 11 October at 14:34 UTC; (c) a strip of SAR data extracted across the ocean-pancake edge along the main direction of the wave energy, and (d) the five $7.68 \text{ km} \times 7.68 \text{ km}$ imagettes into which the strip was divided; (e) the observed SAR spectra for the extracted (left) sea-ice (1 to 3) and (right) open water (4 and 5) imagettes. Units are wavenumber $K_x/\Delta K$ and $K_y/\Delta K$ with $\Delta K = \pi/8 \cdot 10^{-2} \text{ rad m}^{-1}$. The circles correspond to peak wavelength $\lambda = 50 \text{ m}$ and 100 m . The top of the images is not due north but a direction at right angles to the incoming major wave vector.

This technique has been also tested for ESA Sentinel-1 SAR products [13], and adapted for Antarctic coastal polynyas with excellent results [15]. Although it is evident that further validation activities should be conducted, the technique could now be employed for mass flux estimates from coherent icefields of frazil-pancake ice in the Arctic, along the Antarctic ice edge, and across coastal polynyas.

A processing scheme was also developed for rapid measurement of pancake ice size distribution from aerial photographs [16]. This scheme comprises several steps, including a non-linear support vector machine analysis, a marker-controlled watershed segmentation, and the final ice size distribution computation. This tool is expected to be used for retrieving immediate information on pancake size

distribution during field campaigns, and for improving the validation of the SAR-derived pancake ice information.

2.3. Determination of Risk Index Outcome (RIO) of International Maritime Organization (IMO) Polar Code with CryoSat-2 SAR Interferometer Radar Altimeter (SIRAL) Data

Traditionally, ice services provide information on SIT, SIC, degree of ridging, and the fraction of different ice types. The ship operators then assess navigability using this information. A new product developed in SPICES seeks to address navigability more directly. More precisely, it responds to the requirements for a specific ship ice class in certain ice conditions as set by the International Code for Ships Operating in Polar Waters formulated by the IMO (IMO Polar Code) [17,18]. The Polar Code defines RIO as a numeral between -30 and 30 that represents the risk for ship of a given ice class to suffer damage from sea ice [18] with a smaller number representing greater risk. The POLARIS system, which belongs to the Polar Code, gives design rules for seven different polar classes (PC) of ships ranging from the strongest, PC1, to the weakest, PC7. As the same ice conditions pose very different risk to ships depending on their PC, the RIO numeral is a function of both PC and ice conditions. For each PC, different ice types are assigned a risk value. Naturally similar ice will pose a larger risk for weaker ships. A lookup table of risk values for different stages of ice development [1] used in operational ice charts is given in [18], and the RIO numeral is defined to be mean risk value weighted by partial SICs.

RIO is designed to be a decision-making tool with thresholds at $\text{RIO} = 0$ and $\text{RIO} = -10$. For tactical navigation this means there are three outcomes—normal operations, restricted operations or operations not permitted. We use the decisions “go,” “go with restrictions,” and “no-go” for the three cases respectively. A positive RIO value indicates an acceptable level of damage risk (“go”). If the value is from -10 to zero then the risk is too high unless compensated by other means, such as limiting the ship speed or using icebreaker assistance “go with restrictions”. When RIO is below -10 , the risk is too large and the ship should not enter the ice (“no-go”). In other words, instead of trying to derive exact RIO numeral from satellite data, our method provides a decision for different PCs.

The SPICES RIO product is based on the ice type classification by CryoSat-2 SIRAL waveform data [19,20]. As presented in [19], the SIRAL echo waveform is sensitive to large scale surface roughness, which in turn is correlated with the harshness of ice conditions and risk to ships. Young thin ice is smooth, resulting in a narrow and peaky waveform whereas thick deformed ice will result in more diffuse waveforms. Instead of the modified WMO ice types used in [19], we classify waveforms into three RIO decision classes. We characterise the waveform using four parameters (pulse peakiness, leading edge width, left tail to peak ratio and stack standard deviation) that we use as features in our classifier.

RIO decision classes, as defined in the Polar Code, were calculated from operational ice charts. As training material, RIO decision classes derived from Canadian Ice Service ice charts were used here, and a k-nearest neighbours (kNN) classifier for the Polar Classes PC4–PC7 was built to derive RIO decision class outside the training area and period. Here, PC4 is the strongest class suitable for year-round navigation in Arctic FYI, while weaker PC6 and PC7 correspond reasonably well to the Finnish–Swedish ice classes IA Super and IA applied in the Baltic Sea. Classes PC1–PC3 suitable for MYI and second-year ice were excluded from our study, because it was hard to find enough training data for the no-go class. The method is robust and applicable to other delay-Doppler radar altimeters, most importantly those onboard Sentinel-3. An example RIO chart is shown in Figure 3.

The RIO decision classes are given in 25 km resolution along the CryoSat-2 orbit ground track for the winter months of October–April (see RIO charts at <http://ice.fmi.fi/>). The results were validated for January–April 2017 by comparing them with RIO decision classes calculated from the ice charts of the Russian Arctic and Antarctic Research Institute (AARI). For PC5 the results from the classifier were especially good and up to 0.95 correlations were found with the AARI ice charts in January, although this grew worse over time, reaching a minimum of 0.7 in April [20]. For PC7 the correlation was at its

best in April (0.8) and worst in February (0.6). However, the overall spatial distribution of heavy ice was similar in both the AARI ice charts and our products.

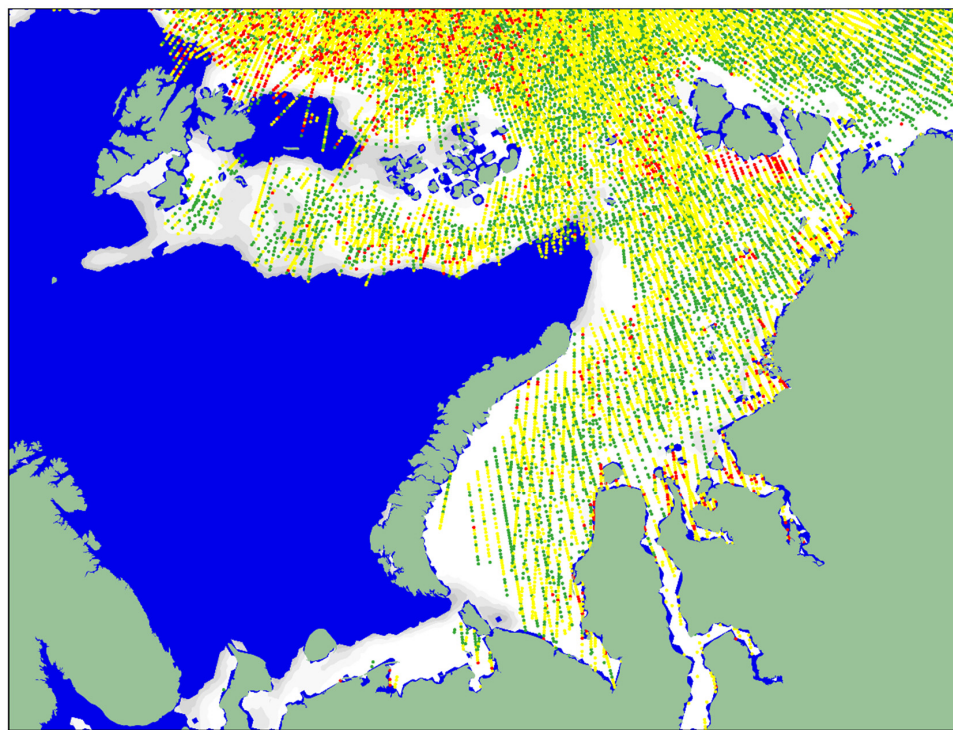


Figure 3. Estimate of risk index outcome (RIO) for the ship of polar class 5 in the Kara Sea. The analysis is based on CryoSat-2 SAR Interferometer Radar Altimeter (SIRAL) observations from 1 March to 1 April 2017. Colour code: red = Operations not permitted, yellow = Operations restricted, green = Operations allowed. White area shows the ice extent from EUMETSAT Ocean and Sea Ice Satellite Application Facility (OSI SAF) SIC product on 1 March 2017.

The current RIO product can be used in the ship navigation. The quality of PC5 decision class estimates in particular were found to be very good. However, there is still room for improvement for weaker ice classes (PC6 and PC7). Importantly, large-scale anomalous ice conditions, such as the outflow of heavy ice from the central Arctic towards the Siberian shelf in early 2017, are easily detectable in our RIO product.

2.4. Thin Ice Thickness from Combined Soil Moisture and Ocean Salinity (SMOS) and Soil Moisture Active Passive (SMAP) Data

Thin sea ice occurs during the freeze-up season over large areas in the marginal ice zone and coastal seas, and in the midwinter season mostly in coastal polynyas and pack ice leads. Ice with a thickness of less than half a meter produces strong heat and salt fluxes, and affects the weather and deep-water circulation in the polar oceans. For ship navigation in sea ice-covered waters, the identification of thin ice areas is naturally essential.

Thin ice thickness estimation in winter conditions can be conducted with the MR data. Algorithms for thin ice thickness retrieval have been developed for high frequency (36 and 89 GHz) MR data in many studies, e.g., [21], but they only apply for high SIC sea ice with up to 20 cm thickness and are sensitive to ice type and ice surface conditions, like snow cover and presence of frost flowers [22,23].

Other studies have shown that MR measurements at low-frequency L-band from ESA's SMOS mission can be used to retrieve SIT of up to 0.5–1.0 m [24–26], where the maximum retrievable SIT depends on ice temperature and salinity. Since 2015, NASA's SMAP mission has been providing T_B data at the same frequency. Within the framework of SPICES, combining T_B data from SMOS

and SMAP for SIT retrieval was investigated [27]. The SIT retrieval follows [25] and is based on the brightness temperature intensity which is the average of the horizontally and vertically polarized brightness temperatures, equal to $0.5(T_{BH} + T_{BV})$. For the combined use of SMOS and SMAP T_B data, the multi-angular SMOS T_B measurements were fit to a SMAP incidence angle of 40° . We found that a two-step regression fitting method by Zhao et al. [28] performs best, yielding a high accuracy even for a small number of measurements. Generally, the two T_B 's agree very well with correlations exceeding 0.99 over sea ice, but they show an intensity bias of about 2.7 K over both ocean and sea-ice regions. When this bias was compensated using a linear fit, a very good agreement between the retrieved SITs was attained, see Figure 4. The main advantages of a combined SIT product are the increased number of daily overpasses leading to an improved data coverage, also towards lower latitudes, as well as a continuation of retrieved time series if one of the sensors stops delivering data.

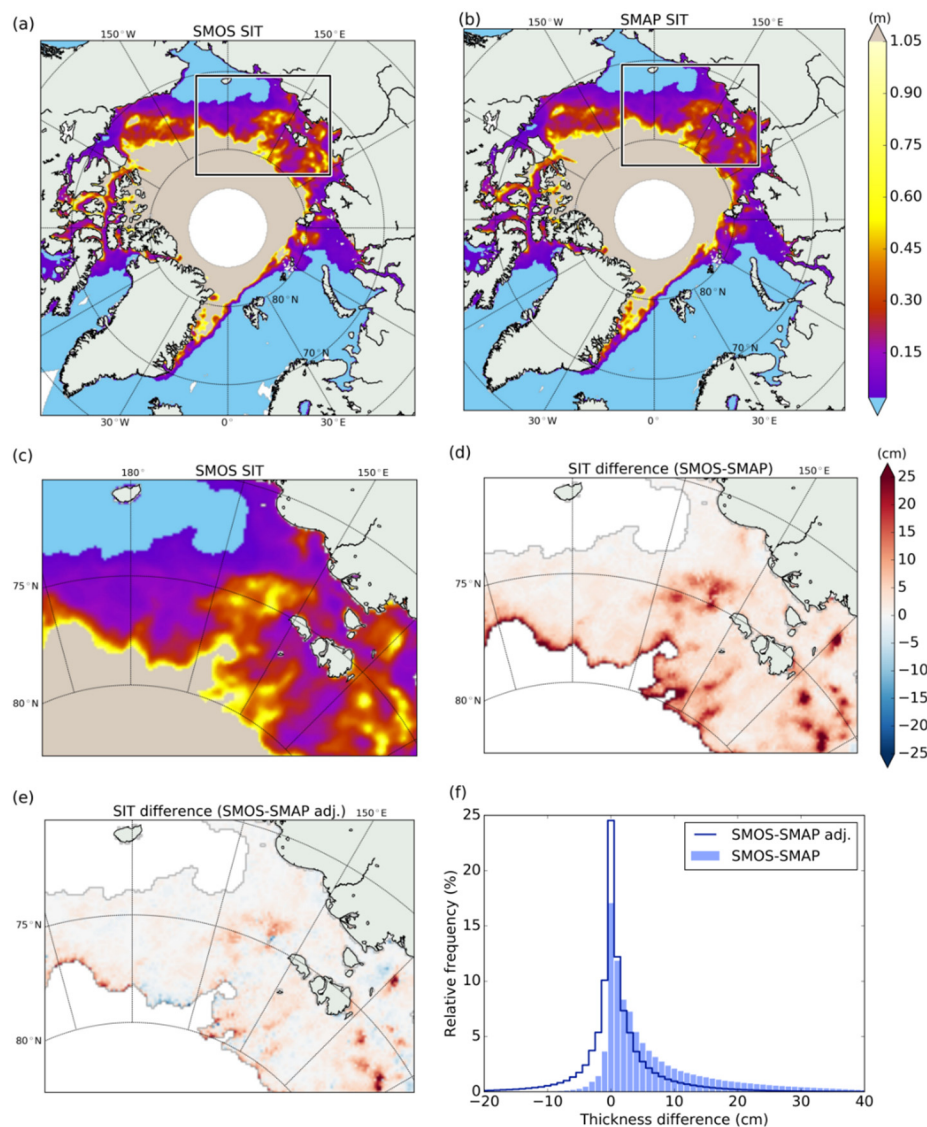


Figure 4. (a) Sea-ice thickness (SIT) on 2 November 2015, derived using T_B 's from Soil Moisture and Ocean Salinity (SMOS) and (b) Soil Moisture Active Passive (SMAP). Grey areas denote saturation of the signal. (c) The rectangle marks the zoom area of SMOS SIT, as well as (d) SIT differences between SMOS and SMAP, and (e) between SMOS and SMAP with adjusted T_B bias. (f) Histogram of SIT differences for all thicknesses between 2 cm and saturation during the winter season of 15 October 2015–15 April 2016 in the Arctic. Figure from [27].

Within the SPICES project, a combined daily SIT dataset from SMOS and SMAP has been produced from 1 April 2015 (first available SMAP data) to 15 April 2015 and for the winter seasons (15 October–15 April) 2015/16 to 2017/18 [29]. Typical SIT uncertainties caused by T_B uncertainties have been estimated to be around 1 cm (or 5%) for 20 cm-thick ice and 4 cm (or 7%) for 65 cm-thick ice [30]. The median maximum retrievable SIT ranges from about 95 cm for cold, low salinity sea ice to about 70 cm for sea ice closer to the melting point.

2.5. Sea-Ice Drift, Thickness and Volume Fluxes Estimation Using Multi-Sensor Satellite Data

Since the 1990s, sea-ice radar backscatter maps have been produced using different scatterometers; recently the Advanced Scatterometer (ASCAT) in the MetOp satellites. Daily data can be found at the CERSAT centre at Ifremer which provides backscatter data and maps over sea ice since 1992 until present using ERS-1/2 (European Remote Sensing satellite), QuikSCAT, NSCAT (NASA Scatterometer), and the ASCATs sensor series [31]. Backscatter intensity over sea ice depends on scatterometer incidence angle and frequency, and sea-ice properties like surface roughness, salinity, temperature, water at the surface. As data from ASCATs are at several incidence angles, backscatter maps are adjusted at a constant incidence angle to ease their interpretation [32]. These daily maps are available at a 12.5 km \times 12.5 km grid at [31]. In SPICES, the backscatter maps have been reprocessed over the entire ASCAT/MetOp-A time series (Jan 2007 onwards), and by merging the MetOp-B data (Oct 2012 onwards).

The backscatter parameter is useful for detecting the sea-ice edge, in particular at the onset of freeze-up. It is also a proxy of sea-ice type, and can be used to estimate sea-ice displacement at coarser grid resolution (62.5 km) [33,34]. Sea-ice motion and type inferred from scatterometer data have been used to estimate FYI and MYI sea-ice volume and export when combined with SIC from MR data and SIT from the merging of the CryoSat-2 SIRAL and SMOS MR data [35].

The 2015–2016 season, with its record low winter ice extent, highlights how the Arctic sea ice becomes more sensitive to climate anomalies due to the loss of MYI. The interannual variability of the relative volume of FYI and MYI as estimated by Ricker et al. [36] highlighted the importance of winter sea-ice growth as a key component. In March 2016 the average Arctic-wide thinning was found to be 10 cm in comparison to the last six-year average, while maximal regional values of 33 cm and 24 cm occurred in the Beaufort Sea and Barents Sea, respectively, see Figure 5. These regional SIT anomalies result from an interplay between ice dynamics and thermodynamics. The Barents Sea SIT reduction seems to be a result of the air temperature increase according to 1948–2016 reanalysis data above 70°N (U.S. National Centers for Environmental Prediction (NCEP) data), whereas the Beaufort Sea reduction seems to be associated with ice volume flux divergence.

This data has also been used to estimate sea-ice volume export through the Fram Strait for the years 2010 to 2017 together with a new CryoSat-2 SIT dataset created by the Alfred Wegener Institute. From these data, Ricker et al. [37] found that the monthly (Oct to Apr) export through the Fram Strait varied between -21 and -540 km 3 . They also show that while the seasonal cycle of Arctic FYI volume is driven by thermodynamic ice growth, 54% of the changes in the Arctic MYI volume over the December–March period can be explained by the ice export through the Fram Strait.

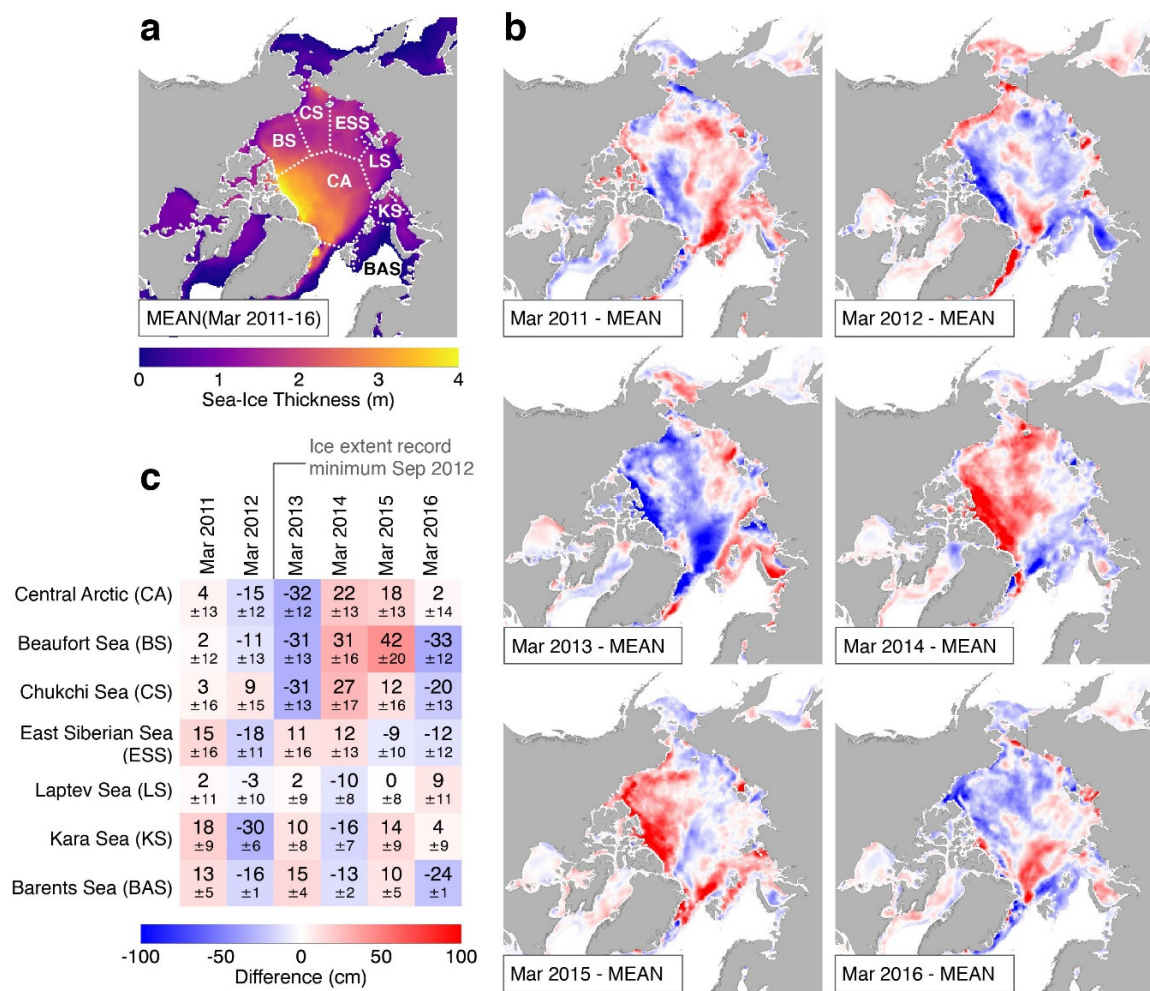


Figure 5. Merged Cryosat-2/SMOS sea-ice thickness (SIT) anomalies for a mean of the weeks in March according to the March SIT averaged over 2011–2016 [36]: (a) March average SIT over 2011–2016, subdivided into maritime domains used in the Multisensor Analysed Sea-Ice Extent (MASIE) product by the U.S. National Snow and Ice Data Center (NSIDC), (b) yearly March SIT anomalies, (c) mean SIT anomalies and uncertainties for each year with respect to the marine domains defined in (a). Figure from [36]. Used with permission from AGU.

2.6. Melt Pond Fraction, Melt Stage, and Sea-Ice Concentration Using SMOS Data

The Arctic summer is the time of rapid sea-ice surface evolution, with surface and lateral sea-ice melt present. It is also the most challenging time for the MR retrievals of sea-ice parameters as they are affected by the liquid water on the sea-ice surface (surface wetness, melt ponds, brine content). The existing SIC retrievals with the MR data are compromised in summer, e.g., [38]. The optical sea-ice retrievals are less affected by the liquid water on sea ice but suffer from cloud contamination which drastically reduces the product coverage.

Within SPICES, the optical and MR retrievals of summer sea ice have been advanced to simultaneous retrievals of MPF and SIC. The new retrieval method Melt Pond Detector 2 (MPD2) has been developed based on the retrieval algorithms developed by Istomina et al. [39] that were applied on optical spectrometer data from MERIS (Medium-Resolution Imaging Spectrometer) on ENVISAT (2002–2012) and OLCI (Ocean and Land Color Instrument) on Sentinel-3 (2016 onwards). MPD2 steps away from the pixel-wise approach of conventional algorithms but uses additional cumulative melting degree day index (CMDD) data inferred from reanalysis air temperature (T_a) to determine the sea-ice albedo. As a result, the MPF, sea-ice albedo and SIC can be determined simultaneously. The CMDD is

also used in a second, new retrieval of MPF and SIC based on the L-band SMOS radiometer data [40]. The aim of this retrieval is to improve the spatial and temporal coverage of the MPF retrievals beyond that of optical data.

Here we focus on the SMOS retrievals. Due to high water absorption at microwave frequencies, these cannot be used to distinguish melt ponds and open water. Therefore, a direct single pixel MPF retrieval from SMOS is impossible when SIC is below 100%. However, using additional T_a and ice drift data, and tracking a SMOS pixel throughout the whole summer accounting for its T_a history can give the necessary boundary conditions and help separating melt ponds and open water in that pixel throughout the given summer.

We use U.S. National Snow and Ice Data Center (NSIDC) v3 drift data to correct for sea-ice drift, NCEP T_a at the surface to calculate the CMDD for each day along the drift track. CMDD is the sum of daily NCEP T_a 's during all previous days of the year along the drift track since 1 May of the given year. CMDD is set to zero when the T_a was negative for more than 1.5 days. SMOS T_B 's and where available optical MPF have been extracted for each day of the drift track as well. A sample of four years of SMOS T_B 's (2011–2014) in summertime (1 May to 15 Sep) extracted along the drift tracks of selected locations in the Laptev Sea in the Transpolar drift, near point Barrow in the Beaufort gyre, North Greenland, and Queen Elisabeth Islands have been used to study the variability of T_B 's, and to attribute it to lateral or surface melt or to open water for separate regions, months and CMDD ranges.

Among the factors affecting SMOS T_B 's of the extracted drift tracks, melt pond evolution is the most important one. The second important factor is the ice break-up and the lateral sea-ice melt, which is the main reason for the gradual SIC decrease during the Arctic summer. The bottom sea-ice melt does not affect SIC directly but increases MPF via the sea-ice freeboard change [41], which then facilitates lateral sea-ice melt. The winds and ocean currents produce internal forces within the sea-ice cover and are responsible for the ice drift and SIC change. This fluctuation of SIC is assumed to be constant in this work.

In the course of summer, as the sea ice rejects brine and melts from below and from above, the brine channels grow and the whole structure of the sea ice becomes porous. The water content within the sea-ice body grows and affects the SMOS T_B 's. The ice also becomes thinner and more prone to break up. The brine is being rejected as the saline sea ice is melting, which makes the melt ponds in the middle of summer become more saline as compared to the early melt ponds originating from the snow meltwater. The percolation blockage [42] which allows melt pond formation in spring when the melt pond water is fresh is not as effective during the extensive melt. Bottom melt reduces the freeboard of the sea ice so that the flooding line moves up and MPF increases again [41]. This mechanism is responsible for the second MPF peak on FYI. As these new melt ponds drain, the porosity of the sea ice has become so high that FYI cannot hold the high MPF which is frequently reached in peak of the melt onset. The increased water content in ice affects the H-polarized T_B (T_{BH}) as well, although not directly connected to surface or lateral melt. At the last stage of melt, the melt ponds melt through and technically become open water, ice floes break apart which increases lateral melt even more, and SIC drops drastically.

We used the four years of the SMOS training data to derive seven categories of Melt Stage Index (MSI), which were selected considering the above described mechanisms and the values of CMDD and SMOS T_B 's [40]:

1. Sea-ice disintegration after short melt period, end phase of thin ice melt: high water content inside ice, high open water fraction, ponds melt through, high MPF.
2. Melt onset (if CMDD = 0 all the time before): water content inside ice is low, low lateral melt, surface MPF increases; or melt after cold spell (if CMDD was positive before): water content in ice high, high lateral melt, MPF potentially high.
3. Stable melt on dense sea ice: water content within ice low, moderate lateral melt, MPF is the main cause of T_B change.

4. Stable melt after second MPF peak on porous ice: water content within sea ice higher, moderate lateral melt, MPF moderate high.
5. Freeze up or cold spell during summer: most ponds frozen over, ocean assumed open, brine or ocean water within ice present as before.
6. End stage of longer melt: water content in ice high, very strong lateral melt, high surface melt.
7. MYI or drastic melt onset: water content within sea ice low, low lateral melt, T_{BH} reacts to mostly MPF.
8. Open water: ocean or polynya.

This scheme is an extension of the four-stages scheme of Eicken et al. [43]. The numbering of the stages does not indicate the sequence in time. The thresholds of the seven melt stages on CMDD and T_{BH} are shown in Figure 6a.

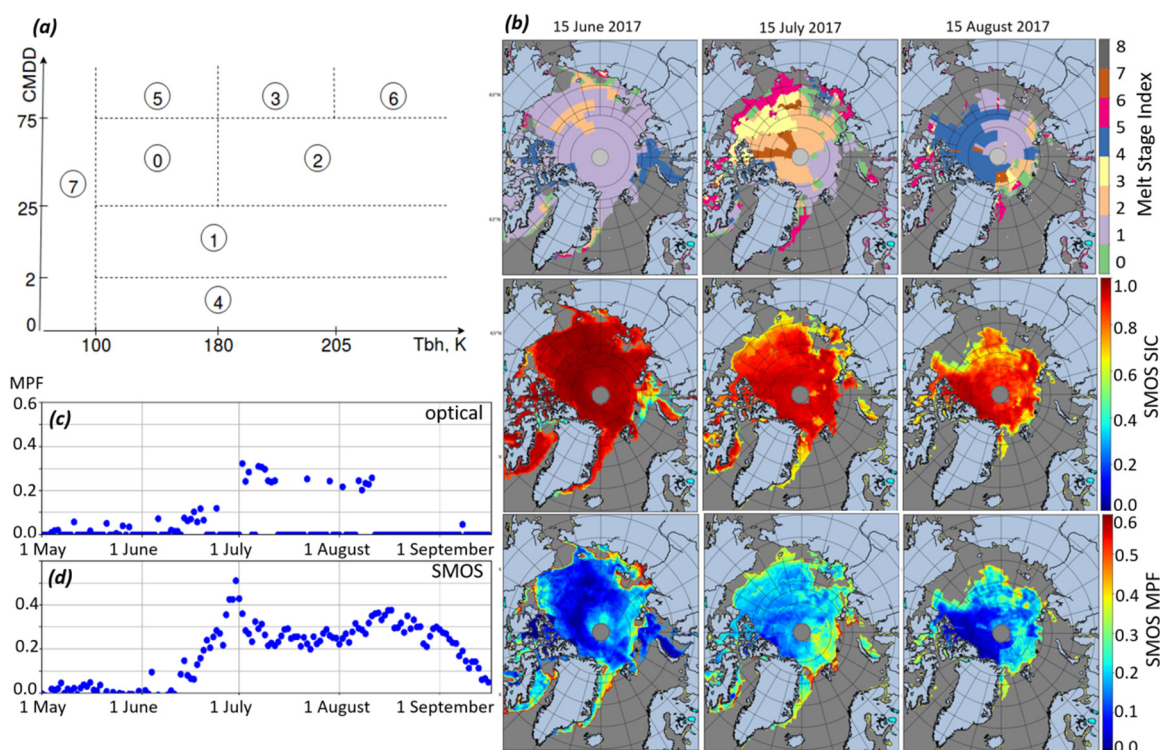


Figure 6. Retrieval of melt pond fraction (MPF) and SIC from the SMOS L-band microwave radiometer (MR) data: (a) thresholds on the T_{BH} and cumulative melting degree day index (CMDD) for seven different melt stages; (b) spatial distribution of retrieved melt stage index (top), SIC (middle), and MPF (bottom) for beginning of melt (15 June), melt evolution (15 July) and end of melt (15 August 2017). (c) Time sequence of the MPF for a selected first-year ice (FYI) region from an optical Melt Pond Detector 2 (MPD2) retrieval, (d) MPF time sequence for the same location from the SMOS retrieval.

The seven MSI categories are applied to determine the role of the surface melt, lateral melt, brine content and sea-ice porosity in the observed T_{BH} of the given ice parcel with the given T_a history. An empirical function derived from summer 2011 of collocated cloud screened SMOS T_{BH} 's of total ice cover and MERIS MPF data [40]:

$$T_{BH} = 252.3 - 167.1 \cdot \text{MPF}, \quad (1)$$

is then used to connect the T_{BH} 's to the total water fraction of the pixel, and the determined MSI melt stage is used to assign the percentage of the lateral vs. surface melt.

An example of the MSI distribution for the three characteristic melt regimes is shown in Figure 6b together with the retrieved SMOS SIC and MPF. Gradual SIC decrease is visible throughout the summer,

whereas the MPF reacts to local temperature changes, e.g., note the freeze-up in the MYI area at the end of summer. A comparison of the SMOS MPF in Figure 6d to the optical MPF product from MERIS for 2011 in Figure 6c shows generally good correspondence between these two MPF products in the cloud-free areas, and an improved coverage of the SMOS MPF product in the areas where clouds prevented optical MPF retrieval.

An extensive validation, comparisons to the existing optical MPF retrievals [44], and case studies with the derived retrievals will enable a variety of applications of the obtained products, e.g., as input to climate models and for the improvement of the existing MR retrievals of the Arctic summer sea-ice surface.

2.7. Snow Depth on Sea Ice Using Microwave Radiometer (MR) Data and Optimal Estimation

Snow on sea ice constitutes an important uncertainty to current SIT retrievals from radar or laser altimetry, yet its spatial and temporal variation remains poorly known. In addition, the snow has important effects on the physical sea-ice system, since a layer of snow changes the sea-ice heat budget by increasing the albedo and acting as an insulating layer. Better knowledge of the spatial and temporal variation of the snow cover is likely to improve the performance of seasonal sea-ice forecasts, both due to its physical effects as well as through its impact on assimilated SITs.

Algorithms for retrieving snow depth from MR data exist (e.g., [45]) but the results are often not very accurate, especially for MYI [46]. Most algorithms are based on the spectral gradient between vertically polarized T_B 's at 19 and 37 GHz, which provide an estimate for the depth of the scattering layer [47], assumed to be equivalent to the snow–ice interface. While this works for snow on FYI, the low salinity and porosity of MYI results in significant penetration into the sea ice, and consequently an overestimation of snow depth. Snow depth estimation over MYI and thick FYI with thick snow cover has been demonstrated using low frequency MR data (SMOS L-band, 6.9 and 18.7 GHz T_B 's) [48,49], but operational and validated products do not yet exist.

In SPICES, a new approach for the snow depth retrieval from MR was developed, and the method was applied to data from the Advanced Microwave Scanning Radiometer 2 (AMSR2). The approach is based on Bayesian inversion of an empirical forward model of sea-ice microwave emissions at multiple frequencies. The forward model consists of a regression-based set of equations containing several physical parameters describing the properties of the sea-ice and snow cover, and extended with an atmospheric component [50]. Regression coefficients were based on collocated spring-time observations and optimized to fit the measured T'_B 's at all available AMSR2 frequency bands (seven frequencies ranging from 6.9 to 89.0 GHz) at V- and H-polarization. Output of the algorithm is a consistent set of values for a range of sea-ice properties, including snow depth. Skill of the algorithm for the snow depth retrieval was evaluated using a Round Robin Data Package containing collocated sets of AMSR2 T_B 's and Operation Ice Bridge (OIB) observations of snow depths along flight tracks [10], with satisfactory agreement between the two.

Pan-Arctic snow depths in April were retrieved for the years 2013–2018. We focused on April snow depths, since the forward model was obtained for spring conditions. Furthermore, spring snow depths are believed to be an important predictor for the start of the sea-ice melt season, and hence for the summer sea-ice extent. We observed significant inter-annual and spatial variability across the Arctic, see Figure 7b, with MYI tending to have the thickest snow cover as it allows snow to accumulate during the entire winter period, see Figure 7a. April snow depths over the last five years were significantly less than the Warren climatological monthly mean [51]. This may, at least partly, result from the decreased area of MYI. The large spatial and temporal variability in snow depth emphasizes the need for maps of monthly snow depth observations, instead of snow depth climatology, when correcting for the snow layer in satellite altimetry SIT retrievals.

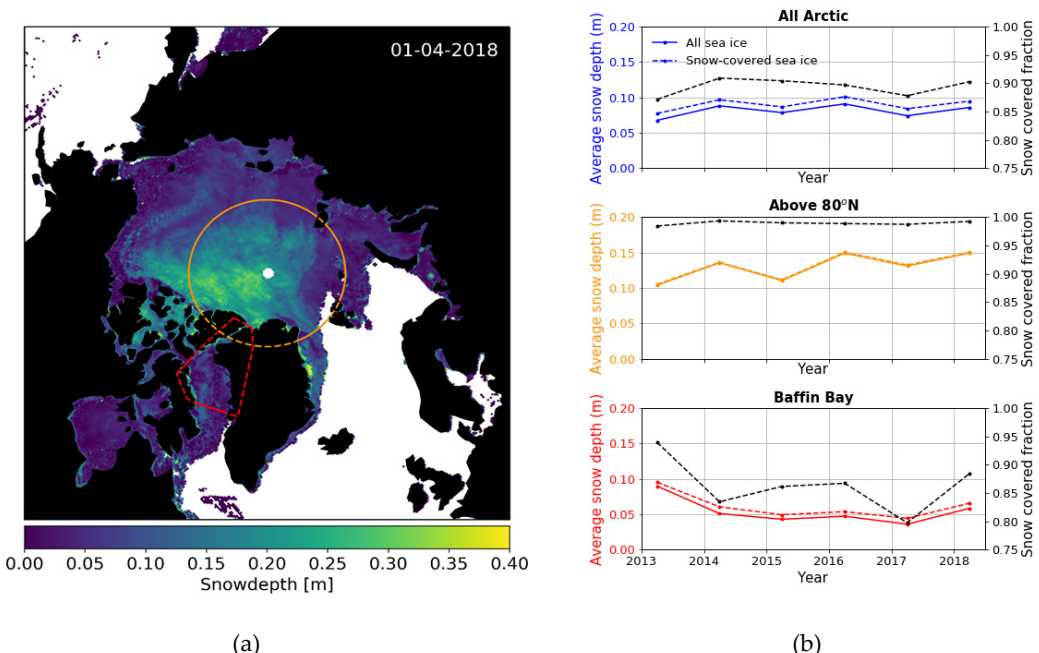


Figure 7. (a) Retrieved snow depths over sea ice on 1 April 2018. The thickest snow is found in high-Arctic regions with multiyear ice (MYI). The two outlined regions are investigated separately (yellow: region above 80°N; red: Baffin Bay). (b) Average snow depths on April 1st during the period 2013–2018. The average value was calculated only for those areas where the sea-ice concentration was above 95% (coloured lines). When calculating the snow-covered fraction of the sea ice (black dashed line), areas with a snow depth less than 1 cm were considered as bare sea ice. The average snow depth was also calculated over only those areas where snow was present (coloured dashed lines).

2.8. Improvements in Predicting Large-Scale Seasonal Sea-Ice Anomalies

At the European Centre of Medium-Range Weather Forecast (ECMWF), global sea-ice forecasts days to seasons ahead are routinely initialized using satellite observations of SIC. This is not yet the case for SIT, although it is arguably at least as important for forecast reliability. The new satellite products of large-scale SIT becoming available from the SPICES project and elsewhere provide exciting opportunities to improve global sea-ice forecasts. Here, the weekly-mean SIT data set CS2SMOS [35] is used to improve the initial conditions of the ECMWF seasonal forecasts [52]. CS2SMOS is derived from CryoSat-2 SIRAL and SMOS L-band MR observations; therefore, it combines the strengths of the two datasets.

A series of data assimilation and re-forecasting experiments have been carried out to demonstrate how seasonal forecasts can benefit from initializing SIT using the C2SMOS product [7]. As Figure 8a shows, forecasts of July sea-ice cover from initial conditions at the beginning of the melt season in May are substantially improved in some regions. Among the regions with the largest improvements are the Kara and East Siberian Seas, so the SPICES results demonstrate an advancement in capability to forecast the navigability in the Northern Sea Route.

The experiments also suggest that improvements are particularly strong for years with extremely low summer sea-ice extents. Figure 8b shows the monthly-mean September sea-ice extent from 2011 to 2016 from observations, as well as from improved SPICES and reference forecasts initialized in July. The SPICES forecasts are on average closer to the observations, which means their overall skill is improved with respect to the reference forecast. However, the largest difference between the forecasts is visible for the extreme low in 2012. The observed value was $3.4 \cdot 10^6 \text{ km}^2$. The ensemble members of the reference forecast spread from 4.6 to $5.5 \cdot 10^6 \text{ km}^2$, and hence provide a very poor forecast of extreme events. For the improved forecasts, ensemble members range from 3.3 to $4.3 \cdot 10^6 \text{ km}^2$, encompassing the observed sea-ice extent of $3.4 \cdot 10^6 \text{ km}^2$.

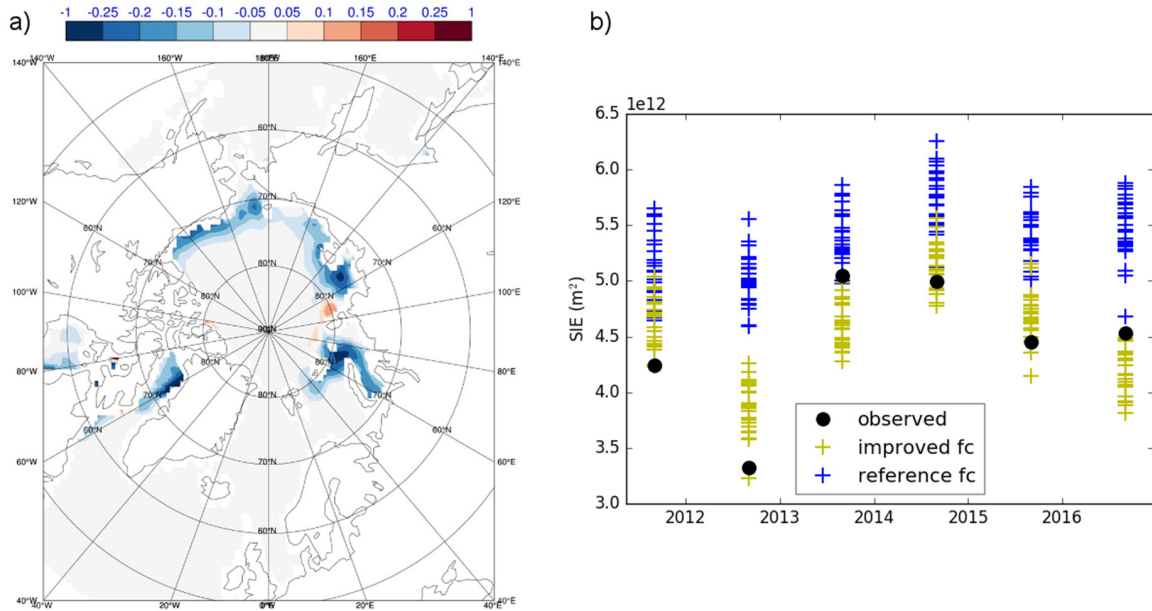


Figure 8. (a) Change of root-mean square error in SIC when forecasting July conditions from May over the period 2011–2016. Blue refers to an improvement in the reforecast experiments initialized with the CS2SMOS SIT observations over the reference forecasts. (b) Monthly-mean sea-ice extent in September from 2011 to 2016 from observations (black dots) and forecasts initialized on 1 July. The reference forecasts are shown as blue crosses, and the Space-borne Observations for Detecting and Forecasting Sea-Ice Cover Extremes (SPICES) forecasts initialized using the CS2SMOS SIT data are shown as yellow crosses. Each cross represents an equally likely realization of the ensemble forecasts.

3. Discussion

The detection, monitoring, and forecasting (both in short and seasonal time scales) of sea-ice conditions and their extremes is very important for ship navigation and offshore activities, and for monitoring of sea-ice processes and trends. For ship navigation and offshore operations, sea-ice information has been available mainly in the form of ice charts, which are based on manual interpretation of available EO-data, mainly SAR imagery, and supporting data like in situ observations and sea-ice models, by ice analysts at national ice services. The charts divide the ice cover into rather large polygons (~10–100 km) to which ice types and properties are assigned. They do not explicitly show in fine resolution the location of hazardous sea-ice conditions (e.g., MYI floes). In addition, the amount of EO-data for sea-ice monitoring is now large, and will increase in the near future. Therefore, there is a need for automated algorithms and systems to produce sea-ice information in fine scale and in near-real-time. Previously, automated algorithms for the SAR data have mostly been developed for ice typing (or stage of ice development), SIC or open water/sea-ice discrimination and sea-ice edge identification [53]. In SPICES, we developed and demonstrated one new SAR product related to sea-ice extreme conditions: estimation of degree of ridging [11], and one new SAR sea-ice product: estimation of pancake ice thickness [13].

Currently, MR and scatterometer data is used to derive global operational sea-ice products showing SIC, FYI and MYI ice types, ice edge, and ice drift. In SPICES we combined multi-sensor satellite data (MR, scatterometer and CryoSat-2) for the estimation of the sea-ice volume in, and export from, the Arctic [35,36]. The sea-ice export through the Fram Strait was found to have large yearly variation, and around half of the changes in Arctic MYI volume in wintertime could be explained by the ice export [37].

Previously, thin ice thickness has been estimated using L-band SMOS MR data [24–26], and daily products are delivered by the Universities of Bremen and Hamburg, but they do not yet have the same level of operational maturity as other sea-ice products (e.g., SIC, ice drift) from the coarse

resolution (~10–25 km) satellite data. Here L-band T_B data from the SMOS and SMAP sensors were fitted together [27] and used for a new SIT product [29,30]. This SIT product is based on an increased number of daily sensor overpasses compared to a SIT product from a single sensor, which allows better data coverage at lower latitudes, and less data loss due to radio frequency interference in the SMOS data.

Snow depth on sea ice can be retrieved operationally with the MR data [45], but the results are often unreliable, especially for MYI [46]. In SPICES, a new method for snow depth retrieval with the MR data was developed and tested. It is based on Bayesian inversion of an empirical forward model of sea-ice surface emission [50]. Using the AMSR2 data, the average pan-Arctic snow depth in April was retrieved. This is believed to be an important predictor for the start of the sea-ice melt season, and hence for the sea-ice summer extent. The spring snow depths were significantly less than the Warren climatological mean [51], which is partly due to the decreasing area of MYI in the Arctic. A large spatial and temporal snow depth variability was observed and, thus, continuous snow depth mapping is needed for the satellite altimetry SIT retrievals.

During the sea-ice melting season, surface wetness and melt ponds have a significant effect on the MR T_B data, decreasing the accuracy of the SIC retrievals. Using optical spectrometer data, MPF can be estimated [39], but the temporal and spatial coverage is heavily restricted by cloud cover. In SPICES we developed simultaneous retrieval of MPF and SIC from L-band SMOS data together with CMDD, ice drift tracking, and a seven-category Melt Stage Index (MSI) [40]. The SMOS-based retrievals have full daily Arctic coverage.

For safe ship navigation in the Arctic and Antarctic, IMO has adopted the Polar Code and related amendments [17,18]. It includes the RIO value, which is a number between –30 and 30 representing the risk of a ship getting damaged by sea ice. The RIO value for a ship can be further classified into “go,” “no-go,” and “go with restrictions” cases. It is envisaged that RIO-based decision-making will become a common practice in ship navigation in ice-covered waters. This requires integrating all available sea-ice information to an operational product which summarizes ice conditions for ship navigation. In SPICES we demonstrated RIO mapping for the Barents and Kara Seas based on the CryoSat-2 SIRAL data. The next step is to add data from other sensors, like SAR and MR, and sea-ice models for RIO maps, which are updated daily over an area of interest.

Currently at ECMWF, global sea-ice forecasts days to seasons ahead are routinely initialized using MR-based SIC. In SPICES, a series of data assimilation and re-forecasting experiments were carried out to demonstrate how seasonal forecasts could benefit from also using the weekly CS2SMOS SIT product in the initialization [7,35]. Forecasts of July sea-ice cover from initial conditions in May showed substantial improvements in some regions. The regions included the Kara and East Siberian Seas, which demonstrate an improvement in forecasting the navigability in the Northern Sea Route. The experiments also suggested that SIT initialization improves seasonal forecasts for years with extremely low summer sea-ice extent.

4. Conclusions

We foresee a wide variety of potential end users for the new SPICES sea-ice products (both EO-based products and sea-ice forecasts), ranging from scientific (sea-ice research and modelling, climate change monitoring and modelling) to governmental (national ice services, numerical weather prediction, icebreaker management, Arctic policy, search and rescue, environment protection, supporting Arctic communities), and further to commercial ones (ship navigation, offshore operations, fishing, tourism). The SPICES sea-ice products have a demonstration level of maturity, and with a reasonable amount of further work, validation, and the setting up of operational product generation environments, they can be integrated into operational service chains by the European Organisation for the Exploitation of Meteorological Satellites (EUMETSAT), national ice services, the Copernicus Marine Environment Monitoring Service (CMEMS), the Copernicus Climate Change Service (C3S), and so on. The new SPICES algorithms can be applied to many forthcoming satellite sensors, e.g., Copernicus Imaging

Microwave Radiometer (CIMR), and Copernicus Polar Ice and Snow Topography Altimeter (CRISTAL). Possible scientific and commercial innovations are tied to the needs of different stakeholders using polar sea-ice products in their operations.

Author Contributions: All authors contributed to the writing and editing of the manuscript. Project administration, J.H. and M.M.; formal analysis and investigation, all authors. All authors have read and agree to the published version of the manuscript.

Funding: This work was supported by the project SPICES (Space-borne Observations for Detecting and Forecasting Sea-Ice Cover Extremes), funded by the European Union's Horizon 2020 Programme (grant agreement No. 640161).

Conflicts of Interest: The authors declare no conflict of interest.

Abbreviations

The following abbreviations and symbols and used in this manuscript:

AARI	Arctic and Antarctic Research Institute
AMSR2	Advanced Microwave Scanning Radiometer 2
ASCAT	Advanced Scatterometer in MetOp satellites of EUMETSAT
CS2SMOS	combined sea-ice thickness product from CryoSat-2 and SMOS data
C3S	Copernicus Climate Change Service
CIMR	Copernicus Imaging Microwave Radiometer
CMDD	cumulative melting degree day index
CMEMS	Copernicus Marine Environment Monitoring Service
CORDIS	Community Research and Development Information Service by European Commission
CRISTAL	Copernicus Polar Ice and Snow Topography Altimeter
DIR	degree of ice ridging
ECMWF	European Centre of Medium-Range Weather Forecast
EO	Earth Observation
ESA	European Space Agency
EUMETSAT	European Organisation for the Exploitation of Meteorological Satellites
FIS	Finnish Ice Service
FYI	first-year ice
HEM	helicopter-borne electromagnetic sensor for sea-ice thickness measurement
IMO	International Maritime Organization
JAXA	Japan Aerospace Exploration Agency
kNN	k-nearest neighbours classifier
MERIS	Medium Resolution Imaging Spectrometer
MPF	melt pond fraction
MPD2	Melt Pond Detector 2
MR	microwave radiometer
MSI	Melt Stage Index
MYI	multiyear ice
NASA	National Aeronautics and Space Administration
NCEP	U.S. National Centers for Environmental Prediction
NSCAT	NASA Scatterometer
NSIDC	U.S. National Snow and Ice Data Center
NWP	numerical weather prediction
OIB	Operation Ice Bridge
OLCI	Ocean and Land Color Instrument
PC	polar class of a ship in IMO Polar Code
RIO	risk index outcome in IMO Polar Code
SAR	synthetic aperture radar
SIC	sea-ice concentration
SIRAL	SAR Interferometer Radar Altimeter
SIT	sea-ice thickness
SMAP	Soil Moisture Active Passive satellite

SMOS	Soil Moisture and Ocean Salinity satellite
SPICES	Space-borne observations for detecting and forecasting sea-ice cover extremes, project by the EU's Horizon 2020 programme
WMO	World Meteorological Organization
T_a	air temperature
T_B	brightness temperature
T_{BH}	H-polarized brightness temperature
T_{BV}	V-polarized brightness temperature

References

1. JCOMM Expert Team on Sea Ice. *Sea-Ice Nomenclature: Snapshot of the WMO Sea Ice Nomenclature* WMO No. 259; World Meteorological Organization: Geneva, Switzerland, 2014; p. 121.
2. Dirkson, A.; Denis, B.; Merryfield, W.J. A multimodel approach for improving seasonal probabilistic forecasts of regional Arctic sea ice. *Geophys. Res. Lett.* **2019**, *46*, 10844–10853. [[CrossRef](#)]
3. Melsom, A.; Palerme, C.; Müller, M. Validation metrics for ice edge position forecasts. *Ocean Sci.* **2019**, *15*, 615–630. [[CrossRef](#)]
4. Zampieri, L.; Goessling, H.F.; Jung, T. Bright prospects for Arctic sea ice prediction on subseasonal time scales. *Geophys. Res. Lett.* **2018**, *45*, 9731–9738. [[CrossRef](#)]
5. Notz, D.; Jahn, A.; Holland, M.; Hunke, E.; Massonnet, F.; Stroeve, J.; Tremblay, B.; Vancoppenolle, M. The CMIP6 Sea-Ice Model Intercomparison Project (SIMIP): Understanding sea ice through climate-model simulations. *Geosci. Model Dev.* **2016**, *9*, 3427–3446. [[CrossRef](#)]
6. Keeley, S.; Mogensen, K. *Dynamic Sea Ice in the IFS*; ECMWF Newsletter, 156; ECMWF: Reading, UK, 2018; pp. 23–29.
7. Balan-Sarojini, B.; Tietsche, S.; Mayer, M.; Alonso-Balmaseda, M.; Zuo, H. *Towards Improved Sea Ice Initialization and Forecasting with the IFS*; ECMWF Technical Memoranda; ECMWF: Reading, UK, 2019.
8. Balan-Sarjojini, B.; Tietsche, S.; Mayer, M.; Balmaseda, M.A.; Zuo, H.; de Rosnay, P.; Stockdale, T.N.; Vitart, F. Year-round impact of winter sea ice thickness observations on seasonal forecasts. *Cryosphere Discuss.* **2020**, in press.
9. Space-Borne Observations for Detecting and Forecasting Sea Ice Cover Extremes | SPICES Project | H2020 | CORDIS | European Commission. Available online: <https://cordis.europa.eu/project/id/640161> (accessed on 12 December 2019).
10. Pedersen, L.T.; Tonboe, R.; Saldo, R.; Heygster, G.; Nicolaus, M.; Ozsoy-Cicek, B. *Reference Datasets*; H2020 SPICES Deliverable: D1.2, D1.3 & D1.4 ; Danish Meteorological Institute: Copenhagen, Denmark, 2016.
11. Gegiuc, A.; Similä, M.; Karvonen, J.; Lensu, M.; Mäkinen, M.; Vainio, J. Estimation of degree of sea ice ridging based on dual-polarized C-band SAR data. *Cryosphere* **2018**, *12*, 343–364. [[CrossRef](#)]
12. Aulicino, G.; Sansiviero, M.; Paul, S.; Cesarano, C.; Fusco, G.; Wadhams, P.; Budillon, G. A new approach for monitoring the Terra Nova Bay polynya through MODIS ice surface temperature imagery and its validation during 2010 and 2011 winter seasons. *Remote Sens.* **2018**, *10*, 366. [[CrossRef](#)]
13. Wadhams, P.; Aulicino, G.; Parmiggiani, F.; Persson, P.O.G.; Holt, B. Pancake ice thickness mapping in the Beaufort Sea From wave dispersion observed in SAR imagery. *J. Geophys. Res. Oceans* **2018**, *123*, 2213–2237. [[CrossRef](#)]
14. Wadhams, P.; Aulicino, G.; Parmiggiani, F.; Pignagnoli, L. Sea ice thickness mapping in the Beaufort Sea using wave dispersion in pancake ice—A case study with intensive ground truth. In Proceedings of the European Space Agency Living Planet Symposium, Prague, Czech Republic, 9–13 May 2016; Volume ESA SP-740.
15. Aulicino, G.; Wadhams, P.; Parmiggiani, F. SAR pancake ice thickness retrieval in the terra nova bay (Antarctica) during the PIPERS Expedition in winter 2017. *Remote Sens.* **2019**, *11*, 2510. [[CrossRef](#)]
16. Parmiggiani, F.; Moctezuma-Flores, M.; Wadhams, P.; Aulicino, G. Image processing for pancake ice detection and size distribution computation. *Int. J. Remote Sens.* **2019**, *40*, 3368–3383. [[CrossRef](#)]
17. IMO. *International Code for Ships Operating in Polar Waters (Polar Code)*; MEPC 68/21/Add.1, Annex 10; IMO: London, UK, 2015.

18. IMO. *Guidance on Methodologies for Assessing Poperational Capabilities and Limitations in Ice*; MSC.1/Circ.15; IMO: London, UK, 2016.
19. Rinne, E.; Similä, M. Utilisation of CryoSat-2 SAR altimeter in operational ice charting. *Cryosphere* **2016**, *10*, 121–131. [CrossRef]
20. Rinne, E.; Sallila, H. *Comparison of Sea Ice Type Estimates from Satellite Radar Altimetry and Auxiliary Sea Ice Type Products*; H2020 SPICES Deliverable D3.3; Finnish Meteorological Institute: Helsinki, Finland, 2017.
21. Iwamoto, K.; Ohshima, K.I.; Tamura, T. Improved mapping of sea ice production in the Arctic Ocean using AMSR-E thin ice thickness algorithm. *J. Geophys. Res. Oceans* **2014**, *119*, 3574–3594. [CrossRef]
22. Nihashi, S.; Ohshima, K.I.; Tamura, T.; Fukamachi, Y.; Saitoh, S. Thickness and production of sea ice in the Okhotsk Sea coastal polynyas from AMSR-E. *J. Geophys. Res. Oceans* **2009**, *114*, C10025. [CrossRef]
23. Shokr, M.; Asmus, K.; Agnew, T.A. Microwave emission observations from artificial thin sea ice: The ice-tank experiment. *IEEE Trans. Geosci. Remote Sens.* **2009**, *47*, 325–338. [CrossRef]
24. Kaleschke, L.; Tian-Kunze, X.; Maaß, N.; Mäkinen, M.; Drusch, M. Sea ice thickness retrieval from SMOS brightness temperatures during the Arctic freeze-up period. *Geophys. Res. Lett.* **2012**, *39*, L05501. [CrossRef]
25. Tian-Kunze, X.; Kaleschke, L.; Maaß, N.; Mäkinen, M.; Serra, N.; Drusch, M.; Krumpen, T. SMOS-derived thin sea ice thickness: Algorithm baseline, product specifications and initial verification. *Cryosphere* **2014**, *8*, 997–1018. [CrossRef]
26. Huntemann, M.; Heygster, G.; Kaleschke, L.; Krumpen, T.; Mäkinen, M.; Drusch, M. Empirical sea ice thickness retrieval during the freeze-up period from SMOS high incident angle observations. *Cryosphere* **2014**, *8*, 439–451. [CrossRef]
27. Schmitt, A.; Kaleschke, L. A consistent combination of brightness temperatures from SMOS and SMAP over Polar Oceans for sea ice applications. *Remote Sens.* **2018**, *10*, 553. [CrossRef]
28. Zhao, T.; Shi, J.; Bindlish, R.; Jackson, T.J.; Kerr, Y.H.; Cosh, M.H.; Cui, Q.; Li, Y.; Xiong, C.; Che, T. Refinement of SMOS multiangular brightness temperature toward soil moisture retrieval and its analysis over reference targets. *IEEE J. Sel. Top. Appl. Earth Observ. Remote Sens.* **2015**, *8*, 589–603. [CrossRef]
29. Schmitt, A.; Kaleschke, L. Combined SMOS and SMAP sea ice thickness Arctic (Version 1.0) [Data set]. Zenodo **2018**. [CrossRef]
30. Schmitt, A.; Kaleschke, L. *Gridded Product of Sea Ice Thickness from SMOS and SMAP and Uncertainties*; H2020 SPICES Deliverable D6.3; University of Hamburg: Hamburg, Germany, 2017.
31. CERSAT—Monitoring Sea Ice with Scatterometers. Available online: <http://cersat.ifremer.fr/oceanography-from-space/our-domains-of-research/sea-ice> (accessed on 27 January 2020).
32. Gohin, F.; Cavanié, A. A first try at identification of sea ice using the three beam scatterometer of ERS-1. *Int. J. Remote Sens.* **1994**, *15*, 1221–1228. [CrossRef]
33. Girard-Ardhuin, F.; Ezraty, R. Enhanced Arctic sea ice drift estimation merging radiometer and scatterometer data. *IEEE Trans. Geosci. Remote Sens.* **2012**, *50*, 2639–2648. [CrossRef]
34. Lavergne, T.; Eastwood, S.; Teffah, Z.; Schyberg, H.; Breivik, L.-A. Sea ice motion from low-resolution satellite sensors: An alternative method and its validation in the Arctic. *J. Geophys. Res.* **2010**, *115*, C10032. [CrossRef]
35. Ricker, R.; Hendricks, S.; Kaleschke, L.; Tian-Kunze, X.; King, J.; Haas, C. A weekly Arctic sea-ice thickness data record from merged CryoSat-2 and SMOS satellite data. *Cryosphere* **2017**, *11*, 1607–1623. [CrossRef]
36. Ricker, R.; Hendricks, S.; Girard-Ardhuin, F.; Kaleschke, L.; Lique, C.; Tian-Kunze, X.; Nicolaus, M.; Krumpen, T. Satellite-observed drop of Arctic sea ice growth in winter 2015–2016. *Geophys. Res. Lett.* **2017**, *44*, 3236–3245. [CrossRef]
37. Ricker, R.; Girard-Ardhuin, F.; Krumpen, T.; Lique, C. Satellite-derived sea ice export and its impact on Arctic ice mass balance. *Cryosphere* **2018**, *12*, 3017–3032. [CrossRef]
38. Ivanova, N.; Pedersen, L.T.; Tonboe, R.T.; Kern, S.; Heygster, G.; Lavergne, T.; Sørensen, A.; Saldo, R.; Dybkjær, G.; Brucker, L.; et al. Inter-comparison and evaluation of sea ice algorithms: Towards further identification of challenges and optimal approach using passive microwave observations. *Cryosphere* **2015**, *9*, 1797–1817. [CrossRef]
39. Istomina, L.; Heygster, G.; Huntemann, M.; Schwarz, P.; Birnbaum, G.; Scharien, R.; Polashenski, C.; Perovich, D.; Zege, E.; Malinka, A.; et al. Melt pond fraction and spectral sea ice albedo retrieval from MERIS data—Part 1: Validation against in situ, aerial, and ship cruise data. *Cryosphere* **2015**, *9*, 1551–1566. [CrossRef]
40. Heygster, G.; Istomina, L.; Zege, E.; Malinka, A.; Prikhach, A. *Albedo and MPF Retrieval Methodology Using PM Observations*; H2020 SPICES Deliverable D5.5; University of Bremen: Bremen, Germany, 2018.

41. Polashenski, C.; Wright, N.; Perovich, D.K.; Song, A.; Deep, E.J. The impact of short-term heat storage on the ice-albedo feedback loop. In Proceedings of the American Geophysical Union, Fall Meeting, San Francisco, CA, USA, 12–16 December 2016; Volume C34A-02.
42. Polashenski, C.; Golden, K.M.; Perovich, D.K.; Skillingstad, E.; Arnsten, A.; Stwertka, C.; Wright, N. Percolation blockage: A process that enables melt pond formation on first year Arctic sea ice. *J. Geophys. Res. Oceans* **2017**, *122*, 413–440. [[CrossRef](#)]
43. Eicken, H.; Krouse, H.R.; Kadko, D.; Perovich, D.K. Tracer studies of pathways and rates of meltwater transport through Arctic summer sea ice. *J. Geophys. Res.* **2002**, *107*, 8046. [[CrossRef](#)]
44. Istomina, L.; Heygster, G.; Huntemann, M.; Marks, H.; Melsheimer, C.; Zege, E.; Malinka, A.; Prikhach, A.; Katsev, I. Melt pond fraction and spectral sea ice albedo retrieval from MERIS data—Part 2: Case studies and trends of sea ice albedo and melt ponds in the Arctic for years 2002–2011. *Cryosphere* **2015**, *9*, 1567–1578. [[CrossRef](#)]
45. Comiso, J.C.; Cavalieri, D.J.; Markus, T. Sea ice concentration, ice temperature, and snow depth using AMSR-E data. *IEEE Trans. Geosci. Remote Sens.* **2003**, *41*, 243–252. [[CrossRef](#)]
46. Brucker, L.; Markus, T. Arctic-scale assessment of satellite passive microwave-derived snow depth on sea ice using Operation IceBridge airborne data: Assessment of Snow Depth on Sea Ice. *J. Geophys. Res. Oceans* **2013**, *118*, 2892–2905. [[CrossRef](#)]
47. Comiso, J.C.; Cavalieri, D.J.; Parkinson, C.L.; Gloersen, P. Passive microwave algorithms for sea ice concentration: A comparison of two techniques. *Remote Sens. Environ.* **1997**, *60*, 357–384. [[CrossRef](#)]
48. Maaß, N.; Kaleschke, L.; Tian-Kunze, X.; Drusch, M. Snow thickness retrieval over thick Arctic sea ice using SMOS satellite data. *Cryosphere* **2013**, *7*, 1971–1989. [[CrossRef](#)]
49. Rostosky, P.; Spreen, G.; Farrell, S.L.; Frost, T.; Heygster, G.; Melsheimer, C. Snow depth retrieval on Arctic sea ice from passive microwave radiometers—improvements and extensions to multiyear ice using lower frequencies. *J. Geophys. Res. Oceans* **2018**, *123*, 7120–7138. [[CrossRef](#)]
50. Tonboe, R.; Winstrup, M.; Kreiner, M.; Lavergne, T.; Sørensen, A. *Datasets of Ice and Snow Parameters for Ice Thickness Retrieval and for Input to WP8—Snow Depth on Sea Ice*; H2020 SPICES Deliverable D4.3; Danish Meteorological Institute: Copenhagen, Denmark, 2018.
51. Warren, S.G.; Rigor, I.G.; Untersteiner, N.; Radionov, V.F.; Bryazgin, N.N.; Aleksandrov, Y.I.; Colony, R. Snow depth on Arctic sea ice. *J. Clim.* **1999**, *12*, 1814–1829. [[CrossRef](#)]
52. Johnson, S.J.; Stockdale, T.N.; Ferranti, L.; Balmaseda, M.A.; Molteni, F.; Magnusson, L.; Tietsche, S.; Decremer, D.; Weisheimer, A.; Balsamo, G.; et al. SEAS5: The new ECMWF seasonal forecast system. *Geosci. Model Dev.* **2019**, *12*, 1087–1117. [[CrossRef](#)]
53. Zakhvatkina, N.; Smirnov, V.; Bychkova, I. Satellite SAR data-based sea ice classification: An overview. *Geosciences* **2019**, *9*, 152. [[CrossRef](#)]



© 2020 by the authors. Licensee MDPI, Basel, Switzerland. This article is an open access article distributed under the terms and conditions of the Creative Commons Attribution (CC BY) license (<http://creativecommons.org/licenses/by/4.0/>).